Available online at www.sciencedirect.com
SCIENCE DIRECT®
Journal of Nuclear Materials 321 (2003) 192–209
journal of nuclear materials
www.elsevier.com/locate/jnucmat

The influence of oversized solute additions on radiation-induced changes and post-irradiation intergranular stress corrosion cracking behavior in high-purity 316 stainless steels

L. Fournier [a,*], B.H. Sencer [b], G.S. Was [b], E.P. Simonen [c], S.M. Bruemmer [c]

[a] CEA Saclay, Dept. de Materiaux pour le Nucleaire, Lab. de Caracterisation des Materiaux Irradies, Bat. 625P, 91191 Gif Sur Yvette, France
[b] The University of Michigan, Ann Arbor, MI 48109, USA
[c] Pacific Northwest National Laboratory, Richland, WA 99352, USA

Received 7 February 2003; accepted 21 April 2003

Abstract

The influence of oversized solute additions on the radiation-induced microstructure, radiation-induced segregation (RIS) at grain boundaries and post-irradiation intergranular stress corrosion cracking (IGSCC) behavior of model, high-purity 316 stainless alloys, doped with either 0.3 at.% platinum or 0.3 at.% hafnium, and proton-irradiated to 2.5 and 5 dpa at 400 °C was examined. Radiation-induced microstructure was characterized using both bright and dark field imaging techniques in transmission electron microscopy. Platinum addition was found to promote void nucleation and to increase both the loop density and the mean loop diameter relative to the base alloy at 2.5 dpa. Addition of hafnium was effective in reducing swelling at 2.5 and 5 dpa. Hafnium addition also significantly decreased the mean loop diameter relative to the base alloy. Both platinum and hafnium additions also resulted in significant suppression of RIS at grain boundaries at 2.5 dpa. At 5 dpa, the influence of hafnium addition on RIS was still beneficial but much less pronounced. Comparative constant elongation rate tensile tests performed in a simulated boiling water reactor environment at 288 °C demonstrated a beneficial effect of hafnium addition and to a lesser extent platinum addition on the post-irradiation IGSCC behavior of 316 stainless steel alloys. The 316SS alloy doped with platinum exhibited a slightly lower susceptibility to post-irradiation IGSCC than the 316SS base alloy at both 2.5 and 5 dpa. Most spectacularly, the 316SS alloy doped with hafnium was found to be not susceptible to post-irradiation IGSCC at both 2.5 and 5 dpa. The mechanisms by which oversized solute additions impact point defect behavior as well as the links between radiation-induced changes and irradiation-assisted stress corrosion cracking are discussed.

1. Introduction

Irradiation-assisted stress corrosion cracking (IASCC) of austenitic stainless steel is widely recognized as a critical issue for core internals in all operating light-water reactors (LWRs). IASCC was first identified in the early 1960s in stainless steel fuel cladding. Over the last decades, it became increasingly evident that the problem is very widespread and that many stainless steel core components are susceptible to this form of degradation. In order to meet the needs for higher performance and extended life in the next generation power reactors, in core materials will have to be designed to delay or eliminate IASCC in LWR austenitic alloys. The

* Corresponding author. Tel.: +33-1 6908 9420; fax: +33-1 6908 8552.
E-mail address: fournier@drnsac.cea.fr (L. Fournier).

0022-3115/$ - see front matter © 2003 Elsevier B.V. All rights reserved.
doi:10.1016/S0022-3115(03)00243-5

objective of this work is therefore to develop the scientific basis for a new class of IASCC resistant materials.

IASCC is a complex phenomenon that results from the interactions between irradiation, material, environment and stress [1–3]. Radiation-induced microstructure evolution in the matrix as well as radiation-induced microchemistry evolution at grain boundaries are believed to contribute to IASCC. Both these radiation-induced changes in microstructure and microchemistry are driven by the displacement of atoms from their lattice sites and the subsequent creation of vacancy and interstitial defects that can recombine, agglomerate or migrate to sinks such as free surfaces, grain boundaries, and other interfaces. While displacement of atoms from irradiation cannot be avoided, it is believed that the addition of oversized solute atoms disturbs the processes of recombination, agglomeration and migration of point defects and thereby alters radiation damage [4–11] and possibly IASCC.

Several authors examined the impact of oversized solute additions on radiation-induced changes in microstructure and in microchemistry of austenitic stainless steels. Kato et al. [8] investigated the influence of the addition of 0.35 at.% of various oversized elements (Ti, Zr, Hf, V, Nb and Ta) on both radiation-induced grain boundary segregation (RIS) and void formation in model 316L stainless steel, electron irradiated to 10.8 dpa at temperatures ranging from 400 to 500 °C. Segregation behaviors of Cr and Ni near the grain boundary as well as void formation were strongly affected by the addition of the oversized solute. Hf and Zr addition were found to completely suppress void formation and RIS. Further work [10] on the same alloys irradiated with fast neutrons up to 35 dpa in the temperature range 425–600 °C confirmed the beneficial effect of Hf and Zr in suppressing void formation. Shigenaka et al. [5] performed 400 keV He^+ irradiations on type 316L stainless steels with addition of 0.07, 0.21 or 0.41 wt% of Zr up to 3.4 dpa. An almost complete suppression of Cr depletion at grain boundaries when the Zr content is higher than 0.21 wt% was observed. Watanabe et al. [4] by carrying-out 1 MeV electron irradiation on Fe–16Cr–17Ni pure ternary austenitic alloys doped with 0.1Nb also observed a beneficial effect of niobium oversized solute addition on radiation-induced microstructure at doses up to 2 dpa. Niobium addition suppressed the formation of vacancy type clusters below 177 °C and void swelling below 527 °C. Finally, Dumbill and Hanks [11] investigated the effect of Ti and Nb additions (0.18 and 0.44 wt%, respectively) on RIS of type 304 stainless steel irradiated with 46.5 MeV Ni^{6+} ions up to 5 dpa. Ti and Nb additions both resulted in an important reduction of RIS at grain boundary.

While some evidences of the beneficial effect of oversized solute additions on radiation-induced changes in microstructure and in microchemistry are reported in the literature, very little or no literature data dealing with the effect of oversized solute additions on IASCC are available. Kasahara et al. [6] have investigated the effect of 0.32 wt% Ti and Nb additions on IASCC of 316L stainless steels by means of swelling mandrel type specimens in a boiling water reactor (BWR) up to 2.5×10^{25} n m^{-2} (>1 MeV) at 288 °C. Neither addition of Ti nor Nb was found to improve the IASCC resistance. However, swelling mandrel tests are known to lead to substantial scatter in the data and to require a large number of tests for statistical significance [12].

In this study, the effect of Pt and Hf oversized solute atom additions on radiation-induced microstructure, radiation-induced hardening, radiation-induced microchemistry at grain boundaries and post-irradiation intergranular stress corrosion cracking (IGSCC) resistance of high-purity alloys with a composition representative of 316 stainless steels and proton-irradiated up to 5 dpa is investigated. This complete approach is expected to give new insights into the effects of oversized solute additions on radiation-induced material changes under LWR conditions, since proton irradiation has been demonstrated to reasonably well emulate neutron irradiation effects [13], and establish links between radiation-induced material changes and IASCC in austenitic stainless steels.

2. Experimental procedure

2.1. Materials

Three high-purity, low-carbon, austenitic stainless steel alloys supplied by General Electric Global Research were used in this study. The alloys consisted of a base alloy with a composition representative of a type 316SS, and two alloys with the same base composition but doped with 0.3 at.% platinum (316SS + Pt) or hafnium (316SS + Hf). The compositions of these three alloys are given in Table 1. As received alloys were solution annealed at 1200 °C for 1 h prior to 70% cold working. Cold working was followed by annealing at 900 °C for 20 min and water quenching to obtain a grain size of about 10 μm. As already published elsewhere [14], Hf-rich precipitates with a density of 8.6×10^{20} m^{-3} and a mean size of 25 nm were observed in the 316SS + Hf alloy annealed at 900 °C for 20 min. In order to reduce the Hf-rich precipitate density, 316SS + Hf was annealed at 1100 °C for 30 min instead of 900 °C for 20 min. This heat treatment led to a grain size of about 20 μm, a decrease in the Hf-rich precipitate density to 1×10^{19} m^{-3} as well as an increase in their mean size to 150 nm [15].

Two types of samples were used in the proton-irradiation program: transmission electron microscopy (TEM) bars and SCC specimens. Drawings of sample

Table 1
Chemical composition of the alloys used in this study (in atomic percent)

Alloy	Annealing conditions	Fe	Cr	Ni	Mn	Mo	Si	C	Solute addition
316SS	900 °C for 20 min	Bal.	18.6	13.3	1.2	1.3	0.16	0.09	None
316SS + Pt	900 °C for 20 min	Bal.	18.7	13.4	1.2	1.3	0.16	0.09	0.3% Pt
316SS + Hf	1100 °C for 30 min	Bal.	18.7	13.4	1.2	1.3	0.16	0.09	0.3% Hf

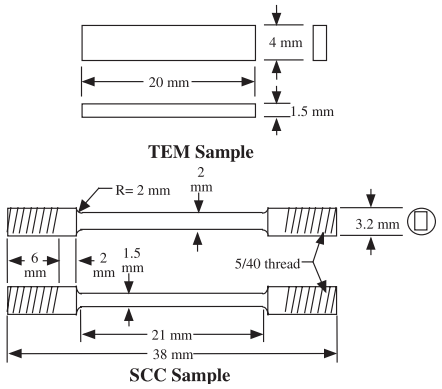

Fig. 1. Schematic of the TEM and SCC specimens used for proton irradiations.

design are provided in Fig. 1. All samples were fabricated by electric discharge machining. Prior to irradiation, specimens were mechanically wet-polished using SiC paper (grit 300–4000) and then electropolished for 3 min in a 60% phosphoric acid – 40% sulfuric acid solution.

2.2. Proton irradiations

Proton irradiations were conducted at the Michigan Ion Beam Laboratory at the University of Michigan. Samples were mounted on a specially designed irradiation stage attached to the main target chamber of a General Ionex Tandetron accelerator. Temperature control was achieved by mounting the samples on a copper block with an indium liquid metal coupling to facilitate heat conduction between the samples and the stage. The sample temperature during irradiation was maintained at 400 ± 10 °C. Irradiations were conducted to nominal doses of 2.5 and 5 dpa at 400 °C with 3.2 MeV protons at a dose rate of approximately 8.5×10^{-6} dpa/s, resulting in a nearly uniform damage rate throughout the first 35 μm of the proton range (~40 μm). Details of the irradiation technique are given in Ref. [16].

The temperature for proton irradiations was chosen to partially compensate for the damage-rate difference and to produce irradiation damage in materials relevant to LWR cores. Experimental doses and dose rates were calculated using TRIM97. As recommended in ASTM E 521-89 [17], a displacement energy of 40 eV was used for all doses and dose-rate calculations.

2.3. Hardening and microstructure characterization

Hardening in proton-irradiated samples was measured by Vickers indentation (MICROMET II) with a load of 25 g. This low load was used to confine the plastic zone ahead of the indenter tip to a depth within the proton range (~40 μm) to ensure that non-irradiated material is not being sampled. Samples for hardness testing were mechanically wet-polished using SiC paper (grit 300–4000) and then electropolished for 3 min in a 60% phosphoric acid – 40% sulfuric acid solution. A total of 20 hardness indents was made for each irradiation condition.

Three-mm TEM discs were cut using a slurry drill cutter. TEM discs were then prepared by electropolishing in a 5% perchloric acid and 95% methanol solution at −65 °C for an applied current between 15 and 18 mA.

Radiation-induced microstructure was characterized using a JEOL2000FX TEM. The dominant microstructural features observed for all specimens were faulted dislocation loops and voids. Faulted dislocation loops were imaged by the rel-rod technique [18]. About 400 faulted dislocation loops were imaged for each irradiation/material condition to obtain average loop diameter and number density. Voids were imaged using Fresnel contrast. About 400 voids were counted to obtain an average void diameter and number density. Four different areas were examined to determined the loop and void diameters using 100,000 × magnification. Thickness measurements were done using convergent beam electron diffraction (CBED) and sometimes thickness fringes when CBED was not possible.

2.4. Microchemistry characterization

Microchemical analysis was performed using a Philips CM200/FEG scanning TEM with energy-dispersive X-ray analysis (STEM/EDS) at Oak Ridge National Laboratory. The CM200/FEG produces a probe approximately ~0.8 nm (full-width, half-maximum) in diameter while operating at 200 kV. A Philips Compustage, room-temperature double-tilt specimen holder was used to minimize specimen drift during analysis. Prior to

analysis, TEM specimens were plasma cleaned using a Southbay PC150 plasma cleaner in both an argon and an oxygen plasma to minimize sample contamination during room-temperature analysis. STEM/EDS measurements were performed on grain boundaries oriented 'edge-on' to the incident electron beam so as to minimize broadening of the boundary profile. Spectral acquisition and analysis was done using EMiSPEC ESVision microscope control and data analysis software. Matrix compositions were taken in each grain (corresponding to the boundaries analyzed) at distances greater than 50 nm from the boundary. Raw intensity data were then converted to weight percents using k-factors calculated from comparison of EDS determined matrix intensities to the bulk alloy composition listed in Table 1.

On each specimen examined, two different grain boundaries were analyzed. During typical analysis of each grain boundary, five composition profiles were taken. In addition to the composition profiles, six spot measurements were taken on each boundary along with six spot measurements of the matrix composition which were used to determine k-factors. Finally, a matrix composition was taken from an area scan at low magnification for each grain to ensure that the spot matrix measurements did not contain artifacts due to local variations in the matrix composition.

2.5. Stress corrosion cracking tests

Constant elongation rate tensile (CERT) tests were conducted in 9 MPa water at 288 °C at a strain rate of 3×10^{-7} s^{-1} in an autoclave system capable of straining four specimens in parallel, providing identical environmental conditions. Inlet conductivity was controlled via automatic additions of dilute H_2SO_4, so that the outlet conductivity was maintained at 0.2 μS/cm. A dissolved O_2 concentration of 2 ppm was controlled by continuously bubbling a mixture of 5% O_2 in argon through a glass mixing column in order to simulate BWR normal water chemistry (NWC). The load on each specimen was monitored independently producing a stress–strain curve for each sample.

Fractographic examination was performed on each specimen following the CERT tests in a Philips XL30/FEG scanning electron microscope. Intergranular (IG) fracture was characterized by measuring both the area of IG facets compared to the area of the fracture surface and the total IG side crack length. Since the proton irradiation only affected the first 40 μm of the irradiated face and IG cracking was only observed in the first 40 μm, the fracture surface was defined by the 40 μm proton penetration depth. This semi-quantitative method was used to compare the relative amount of cracking between the different alloys.

3. Results

Investigations of the influence of Pt and Hf oversized solute addition on radiation-induced microstructure, radiation-induced hardening, radiation-induced microchemistry and post-irradiation IGSCC were carried out in this study. The following results describe the effect of a low concentration of oversized solute atoms on both radiation-induced changes and the post-irradiation IGSCC susceptibility of model, high-purity 316SS.

3.1. Radiation-induced microstructure

The mean faulted loop density, faulted loop diameter as well as void density and void mean diameter were determined for 316SS, 316SS + Pt and 316SS + Hf alloys proton-irradiated to 2.5 dpa and for 316SS and 316SS + Hf proton-irradiated to 5 dpa. Results are summarized in Table 2. Bright-field images of voids and dark-field images of faulted loops after proton-irradiation to 2.5 dpa are displayed in Fig. 2. Bright-field images of voids in the 316SS and 316SS + Hf alloys proton-irradiated to 5 dpa are shown in Fig. 3.

The loop density determined in this study for the high-purity 316SS is consistent with that determined by Gan and Was [19] for high-purity 304SS also proton-irradiated at 400 °C. These densities are lower than those reported by Was et al. [13] for commercial grade 316SS

Table 2
Summary of radiation-induced microstructure characterization (faulted loops and voids) of 316SS, 316SS + Pt and 316SS + Hf alloys proton-irradiated to 2.5 and 5 dpa at 400 °C

Alloy	Dose (dpa)	Loop density (m^{-3})	Mean loop diameter (nm)	Void density (m^{-3})	Mean void diameter (nm)	Swelling (%)
316SS	2.5	9.5×10^{20}	30	1×10^{20}	13	0.01
316SS + Pt	2.5	1.2×10^{21}	38	4×10^{20}	18	0.12
316SS + Hf	2.5	3.1×10^{21}	13	0	0	0
316SS	5	1.5×10^{21}	19	3.5×10^{20}	13	0.04
316SS + Pt	5	No data	No data	No data	No data	No data
316SS + Hf	5	3.9×10^{21}	13	2.4×10^{21}	4	0.01

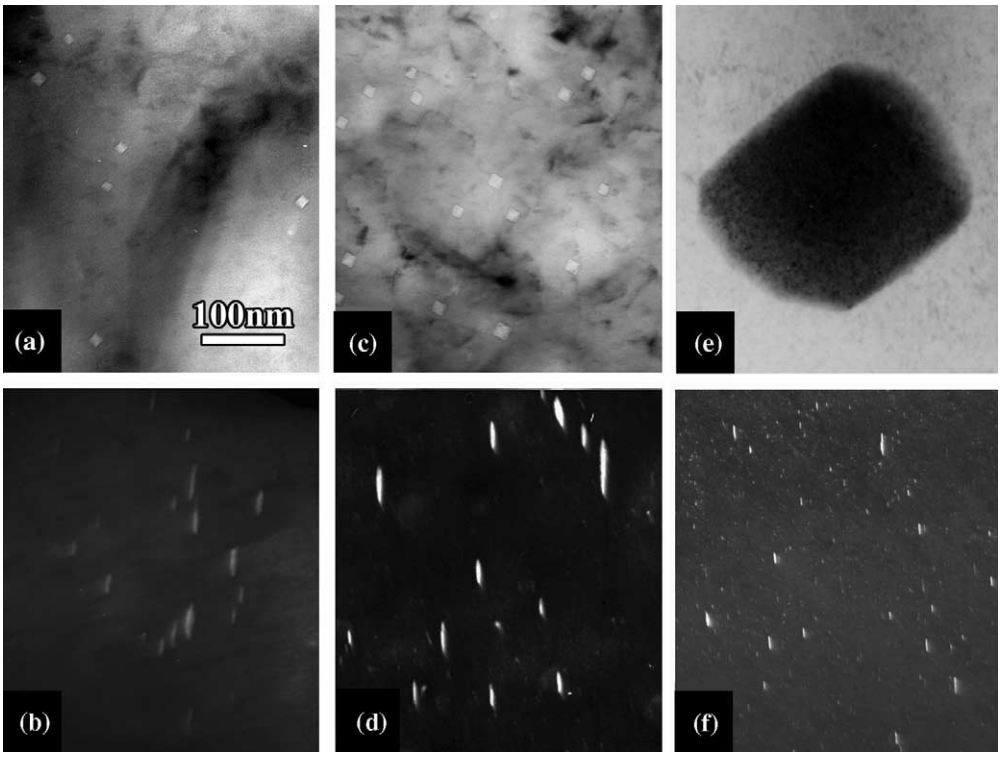

Fig. 2. Bright field images of voids in: (a) 316SS, (c) 316SS + Pt, and (e) 316SS + Hf alloys proton-irradiated to 2.5 dpa at 400 °C as well as dark field images of faulted loops in (b) 316SS, (d) 316SS + Pt, and (f) 316SS + Hf alloys proton-irradiated to 2.5 dpa at 400 °C.

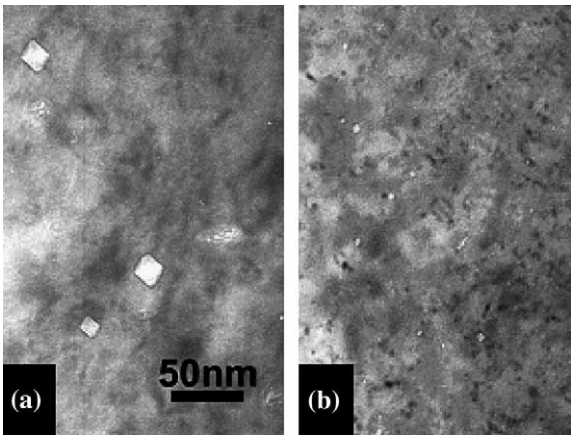

Fig. 3. Bright field images of voids in: (a) 316SS and (b) 316SS + Hf alloys proton-irradiated to 5 dpa at 400 °C.

(10^{22} loops m^{-3}) also proton-irradiated, but at 360 °C. The difference between the loop densities in high-purity SS proton-irradiated at 400 °C and in commercial grade SS proton-irradiated at 360 °C arise from both the irradiation temperature and the chemical composition of the materials. Indeed, Gan and Was [19] showed that, after proton-irradiation, (i) the loop density is increased by a factor of about 3 by decreasing the irradiation temperature from 400 to 360 °C, and (ii) the loop density in a commercial grade alloy is higher than that in a comparable high-purity alloy by a factor of about 3.

The 316SS + Pt alloy exhibits a larger faulted loop size, void density and void size in comparison to the 316SS alloy at 2.5 dpa. This difference in void characteristics resulted in an increased level of swelling (0.13%) in the Pt-doped alloy.

In contrast, Hf addition is shown to have a beneficial effect on radiation-induced microstructure. The 316SS + Hf alloy exhibits a much smaller faulted loop size (13 nm) than the base alloy at 2.5 dpa (30 nm) and no swelling. At the higher dose of 5 dpa, the faulted loop size is also smaller in the 316SS + Hf alloy than in the 316SS alloy. Swelling is also lower in 316SS + Hf alloy proton-irradiated to 5 dpa than in the 316SS alloy proton-irradiated to 5 dpa, confirming the beneficial effect of hafnium addition on radiation-induced microstructure.

3.2. Radiation-induced hardening

The measured hardness of 316SS, 316SS + Pt and 316SS + Hf alloys before and after proton-irradiation to

Table 3
Summary of microhardness measurements on proton-irradiated 316SS, 316SS + Pt and 316SS + Hf alloys to 2.5 and 5 dpa at 400 °C

Alloy	Dose (dpa)	H_V unirr. ($kg\,mm^{-2}$)	H_V irr. ($kg\,mm^{-2}$)	ΔH_V ($kg\,mm^{-2}$)	$\Delta\sigma$ from hardness (Mpa)	$\Delta\sigma$ from microstructure (MPa)
316SS	2.5	167	303	136	483	144
316SS + Pt	2.5	173	258	85	302	226
316SS + Hf	2.5	189	288	99	351	150
3I6SS	5	167	346	179	635	179
316SS + Pt	5	173	285	113	401	No data
316SS + Hf	5	189	252	63	224	250

2.5 and 5 dpa at 400 °C is listed in Table 3. The hardness value of the irradiated condition was subtracted from that of the unirradiated condition to arrive at a hardness increase due to irradiation. The yield strength increase due to irradiation was also estimated using the following empirical relation [20]:

$$\Delta\sigma = 3.55\Delta H_V, \tag{1}$$

where $\Delta\sigma$ is the increment in yield strength (MPa), and ΔH_V is the increment in hardness ($kg\,mm^{-2}$). For the 316SS alloy, the hardness increase at 2.5 dpa was determined to be 136 $kg\,mm^{-2}$, corresponding to an estimated increase in the yield strength of 483 MPa. Interestingly, both 316SS + Pt and 316SS + Hf alloys proton-irradiated to 2.5 dpa exhibit a significantly smaller increase in hardness than the 316SS alloy at 2.5 dpa.

Further hardening is observed in both the 316SS and the 316SS + Pt alloys with an increase in the dose. For the 316SS alloy, the hardness increase at 5 dpa was determined to be 179 $kg\,mm^{-2}$, corresponding to an estimated increase in the yield strength of 635 MPa.

The yield strength increase derived from hardness measurements was also compared with the yield strength increase determined from microstructural characterization using the dispersed barrier hardening model [25]:

$$\Delta\sigma = 3.06\alpha\mu b(\mathrm{Nd})^{0.5}, \tag{2}$$

where $\Delta\sigma$ is the increment in yield strength (MPa), α is the strength of the barrier, μ is the shear modulus (76 GPa), b is the Burgers vector (0.255 nm), N is the barrier density and d is the size of the barrier. When both voids and faulted loops are present in the microstructure, the yield strength change is calculated using the following relation:

$$\Delta\sigma = [(\Delta\sigma_{\mathrm{Loops}})^2 + (\Delta\sigma_{\mathrm{Voids}})^2]^{0.5}, \tag{3}$$

where α is 1.0 for voids and 0.4 for faulted loops [19].

As shown in Table 3, the calculated yield strength changes from measured microstructure using the dispersed hardening model are in poor agreement with the calculated yield strength changes from measured hardness. In fact, using the dispersed hardening model leads to an important underestimation of the radiation-induced yield change.

Gan and Was [19] performed a similar analysis on commercial purity 304SS and 316SS proton-irradiated at 360 °C to doses up to 5 dpa. They observed a good agreement between the calculated yield strength changes from measured microstructure using the dispersed hardening model and the calculated yield strength changes determined from measured hardness at low doses, typically below 1 dpa. Conversely, they observed a poor agreement between the calculated yield strength changes from measured microstructure using the dispersed hardening model and the calculated yield strength changes determined from measured hardness in the dose range 3–5 dpa. Similar to this study, using the dispersed hardening model led to an important underestimation of the radiation-induced yield change in the dose range 3–5 dpa.

3.3. Radiation-induced microchemistry

The results of grain boundary composition measurements on proton-irradiated 316SS, 316SS + Pt and 316SS + Hf alloys are summarized in Table 4. In addition, typical comparative grain boundary composition profiles for Cr, Fe and Ni are shown in Fig. 4.

Strong RIS of alloying elements and impurities was observed for the 316SS alloy proton – irradiated to 2.5 dpa. Cr, Fe, Mo and Mn concentrations at the grain boundary are depleted while Ni and Si are enriched after irradiation. In good agreement with the evolution of RIS as a function of the dose reported in the literature [21], even stronger RIS was observed for the 316SS alloy proton-irradiated to 5 dpa. The composition profiles of the alloying elements are nearly symmetrical, decaying to near-matrix levels within a few nm (<10 nm) from the grain boundary.

The addition of oversized solutes was found to significantly modify RIS at grain boundaries. As shown in Table 4, RIS was significantly suppressed for the 316SS + Pt alloy and it was almost completely suppressed for the

Table 4
Summary of grain boundary composition measurements on proton-irradiated 316SS, 316SS + Pt and 316SS + Hf alloys to 2.5 and 5 dpa at 400 °C

Alloy	Dose (dpa)	# GB	# GB meas.	Fe	Cr	Ni	Mo	Mn	Si	Pt	Hf
316SS											
Avg. GB comp.	2.5	2	6	63.3	12.4	22	1.4	0.8	0.1		
Bulk comp				65.5	17.5	13.3	2.4	1.3	<0.1		
316SS + Pt											
Avg. GB comp.	2.5	2	6	64.9	15.4	15.7	2	1	<0.1	1	
Bulk comp				65.3	16.9	13.6	2	1.2	<0.1	1	
316SS + Hf											
Avg. GB comp.	2.5	2	6	64.3	15.9	15.6	2.5	1.1	<0.1		0.6
Bulk comp				65	17.1	13.6	2.4	1.3	<0.1		0.6
316SS											
Avg. GB comp.	5	2	6	59	10.8	27.9	1.7	0.6	<0.1		
Bulk comp				65.8	16.8	14.4	1.8	1.2	<0.1		
316SS + Hf											
Avg. GB comp.	5	2	6	63.3	12.3	22.2	1.5	0.7	<0.1		–
Bulk comp				64.6	17.4	14	2.2	1.2	<0.1		0.6

316SS + Hf alloy proton-irradiated to 2.5 dpa. A small amount of segregation is still observed (Fig. 4) on the grain boundary composition profile of the 316SS + Pt alloy proton-irradiated to 2.5 dpa. However, it should be emphasized that the grain boundary composition profiles plotted in Fig. 4 represent typical observations while average grain boundary compositions are given in Table 4. The amount of RIS in the 316SS + Hf alloy proton-irradiated to 5 dpa was significantly lower than in the 316SS alloy proton-irradiated to 5 dpa demonstrating a diminished, yet beneficial effect of Hf addition on RIS at 5 dpa. Indeed, the amount of grain boundary segregation in the 316SS + Hf alloy proton-irradiated to 5 dpa was similar to the amount of grain boundary segregation in the 316SS alloy proton-irradiated to 2.5 dpa.

3.4. Post-irradiation stress corrosion cracking

The results of the CERT tests performed in simulated BWR NWC at 288 °C on irradiated and non-irradiated 316SS, 316SS + Pt, 316SS + Hf alloys are summarized in Table 5. The strain-to-failure, failure location, failure mode, percentage of IG cracking, number of cracks, total crack length in the irradiated regions, and the ratio of total crack length to failure strain were tabulated for each specimen. The percentage of IG cracking refers only to the proton-irradiated area of the fracture surface.

SEM micrographs of the fracture surfaces for non-irradiated 316SS and for 316SS, 316SS + Pt and 316SS + Hf irradiated to 2.5 dpa are displayed in Figs. 5 and 6. Side-surface SEM micrographs of the 316SS, 316SS + Pt and 316SS + Hf alloys proton-irradiated to 2.5 dpa are shown in Fig. 7.

Fracture surfaces for 316SS, 316SS + Pt and 316SS + Hf irradiated to 5 dpa are displayed in Figs. 8 and 9. Side-surface SEM micrographs of the 316SS, 316SS + Pt and 316SS + Hf alloys proton-irradiated to 5 dpa are shown in Fig. 10.

The non-irradiated 316SS alloy did not exhibit environmentally assisted cracking. This sample failed at the largest strain (36%) in a transgranular (TG) ductile mode by microvoid coalescence. In contrast, the 316SS alloy was found to be extremely sensitive to IGSCC after proton-irradiation. Irradiation to 2.5 dpa promoted significant IG cracking (43%) and an overall 12% loss of ductility in comparison to the non-irradiated 316SS. The 316SS alloy proton-irradiated to 5 dpa was found to exhibit slightly more IG cracking (48%) and loss in ductility (19%) than the 316SS alloy proton-irradiated to 2.5 dpa.

The addition of oversized solutes was found to have a strong impact on post-irradiation IGSCC behavior of high-purity 316 stainless steels.

(i) Platinum addition appears to improve the post-irradiation IGSCC behavior of 316SS alloys but IG cracking is still observed after CERT testing. Similarities and differences are identified between the post-irradiation IGSCC behaviour of the 316SS + Pt and 316SS. Both alloys show significant IG cracking during CERT tests and are much more susceptible to IGSCC than the 316SS + Hf alloy. However, the Pt-doped alloy exhibits a smaller number of surface cracks and a reduced

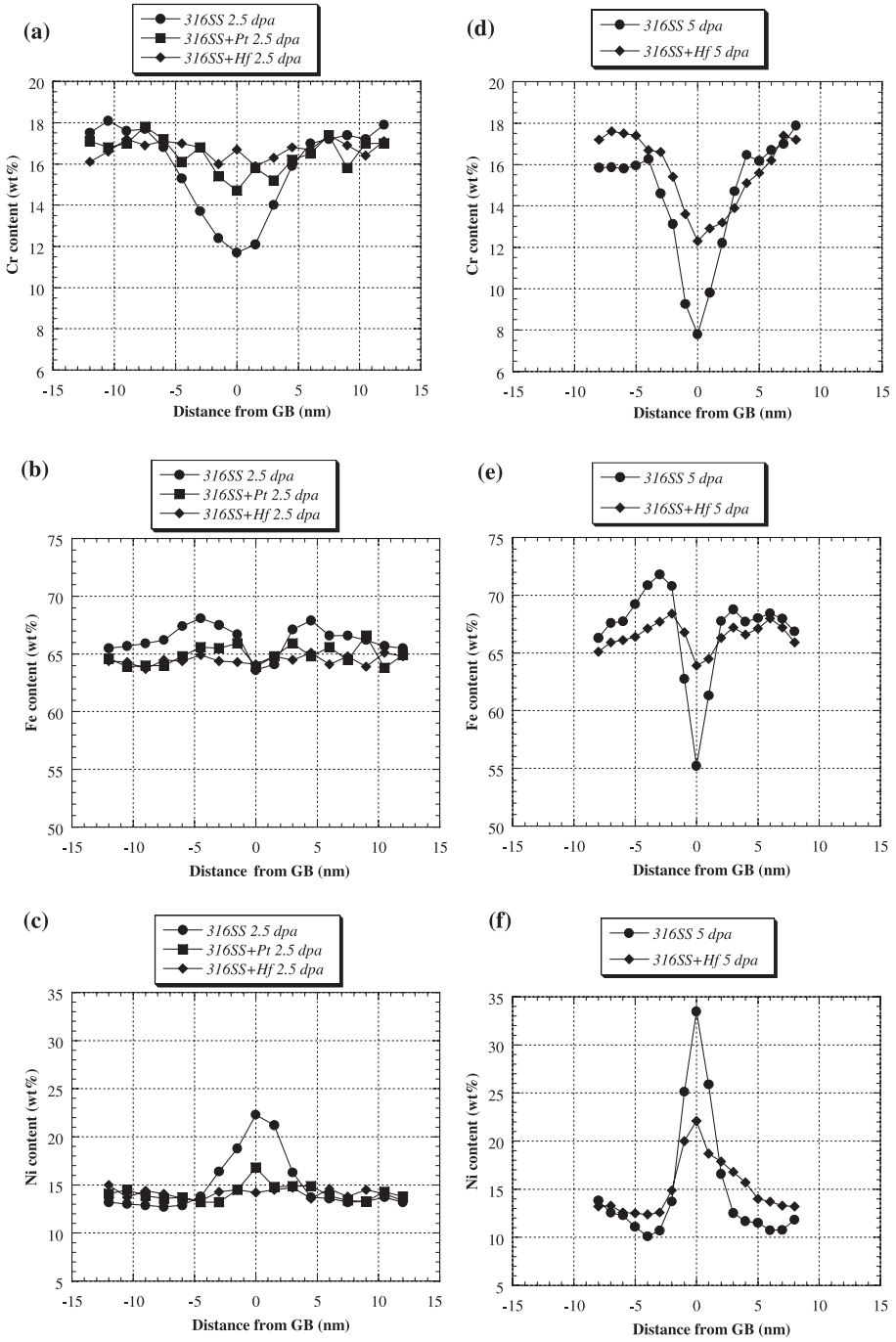

Fig. 4. Comparative (a) Cr, (b) Fe, (c) Ni typical grain boundary composition profiles for 316SS, 316SS + Pt and 316SS + Hf alloys proton-irradiated to 2.5 dpa at 400 °C as well as comparative, (d) Cr, (e) Fe, (f) Ni typical grain boundary composition profiles for 316SS and 316SS + Hf alloys proton-irradiated to 5 dpa at 400 °C.

crack length in comparison to the base alloy. Unexpectedly, the 316SS and 316SS + Pt alloys reveal a similar strain-to-failure at 2.5 dpa, but the Pt-doped alloy exhibits a 10% ductility improvement at 5 dpa. Scatter in the strain-to-failure measurements is not unusual for proton-irradiated specimens and can result from their

Table 5
Summary of CERT tests performed in simulated BWR NWC at 288 °C on non-irradiated 316SS alloy as well as on proton-irradiated 316SS, 316SS + Pt and 316SS + Hf alloys to 2.5 and 5 dpa at 400 °C

Alloy	Dose (dpa)	Strain to failure (%)	Location of failure	Mode of failure	% IG cracking on fracture surface in irradiated region	Number of cracks in irradiated region	Total crack length on irradiated surface (μm)	Total crack length/strain to failure (μm/%)
316SS	–	36		TG ductile	–	–	–	
316SS	2.5	24	Irradiated region	IG + TG ductile	43	11	10 100	421
316SS + pt	2.5	19	Irradiated region	IG + TG ductile	34	4	6100	321
316SS + Hf	2.5	32	Irradiated region	TG ductile	<1	2	1300	41
316SS	5	17	Irradiated region	IG + TG ductile	48	24	22 600	1329
316SS + Pt	5	27	Irradiated region	IG + TG ductile	40	19	11 900	441
316SS + Hf	5	32	Irradiated region	TG ductile	<1	3	1600	50

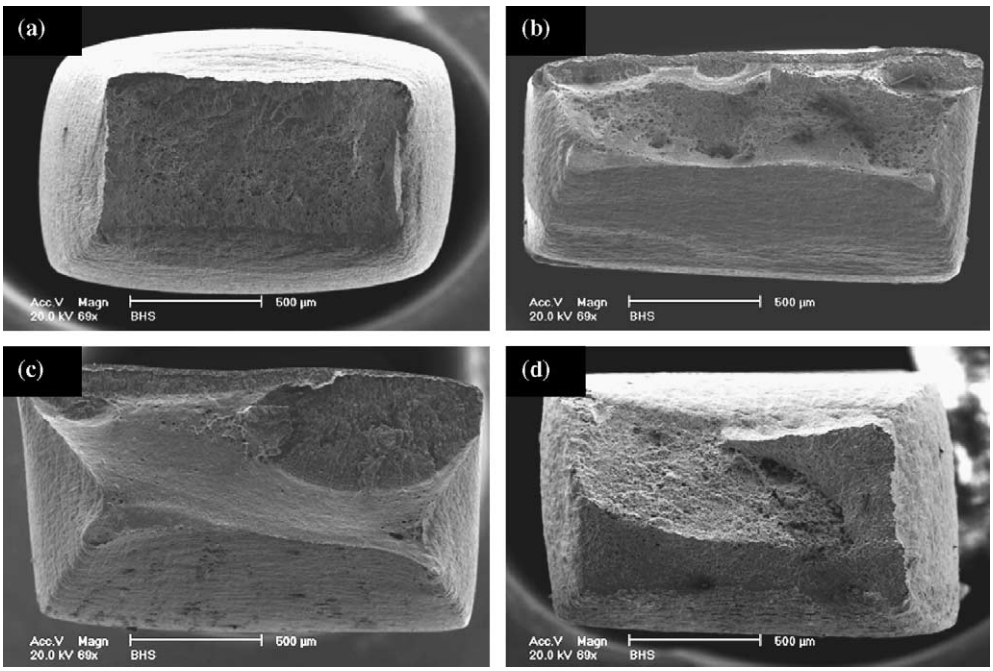

Fig. 5. SEM micrographs of the fracture surface of: (a) non-irradiated 316SS alloy, as well as (b) 316SS, (c) 316SS + Pt and (d) 316SS + Hf alloys proton-irradiated to 2.5 dpa at 400 °C and strained in simulated BWR NWC at 288 °C. The irradiated surface is the top surface in all micrographs.

unique geometry with only 40 μm of the 1500 μm sample thickness being irradiated. IGSCC cracks initiate on the irradiated surface and then progress across the irradiated region of the sample to a depth of 40 μm. Sample failure occurs after the IG crack nucleates a TG crack that propagates either through the thickness of the sample or to a depth where ductile overload results in plastic instability. This process can produce scatter in

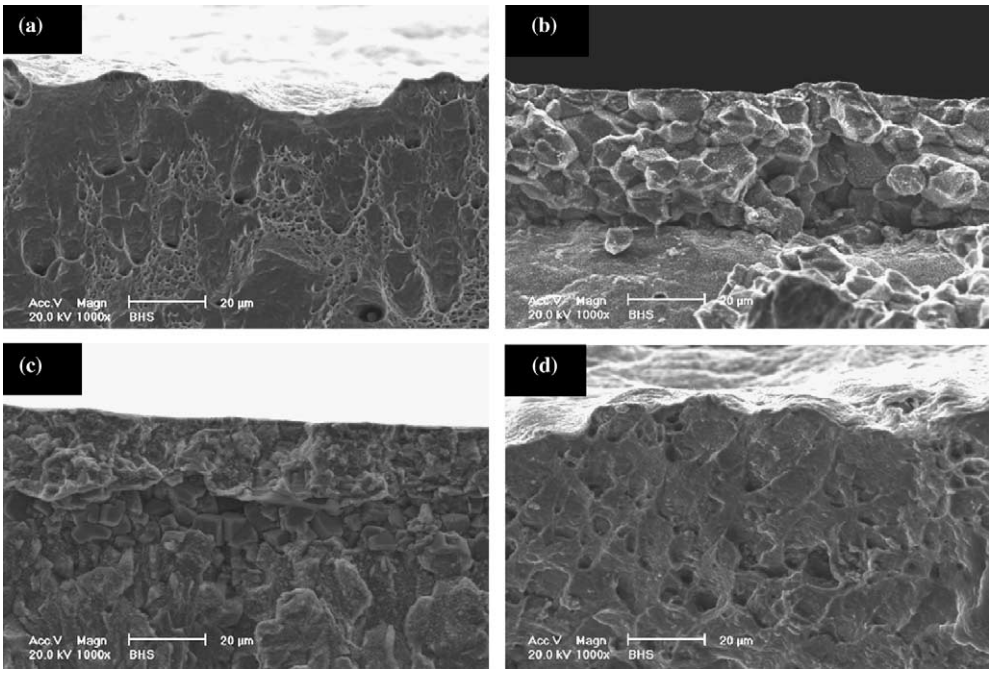

Fig. 6. High magnification SEM micrographs of the fracture surface of: (a) non-irradiated 316SS alloy, as well as (b) 316SS, (c) 316SS + Pt and (d) 316SS + Hf alloys proton-irradiated to 2.5 dpa at 400 °C and strained in simulated BWR NWC at 288 °C. The irradiated surface is the top surface in all micrographs. Notice IG cracking for 316SS alloy and 316SS + Pt alloy.

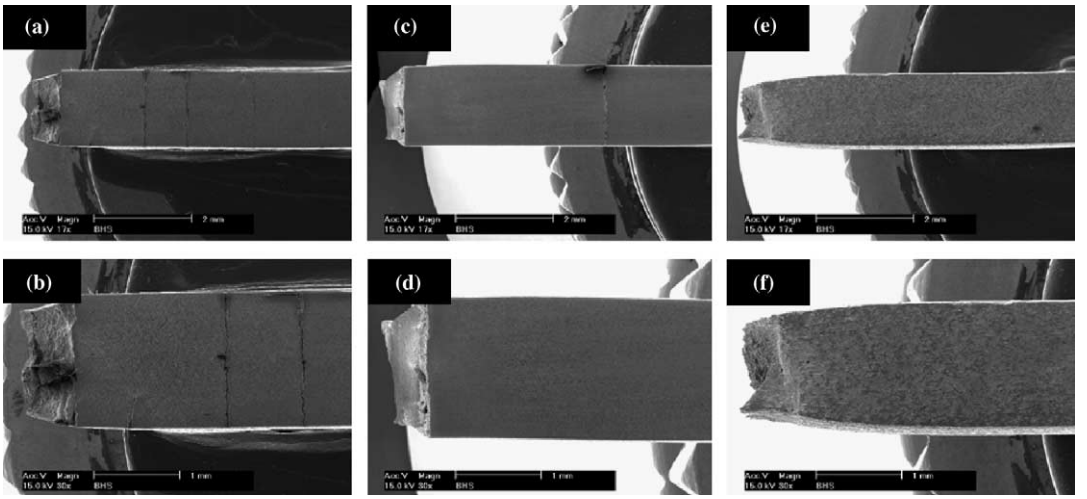

Fig. 7. SEM micrographs of the side surface of (a)–(b) 316SS alloy proton-irradiated to 2.5 dpa at 400 °C, (c)–(d) 316SS + Pt alloy proton-irradiated to 2.5 dpa at 400 °C and (e)–(f) 316SS + Hf alloy proton-irradiated to 2.5 dpa at 400 °C, strained in simulated BWR NWC at 288 °C.

the strain-to-failure data since the total strain is dependent on nucleation and propagation of TG cracks below the irradiated region. The total crack length over the strain-to-failure is therefore considered to better capture the susceptibility of proton-irradiated specimen to IGSCC. At both 2.5 and 5 dpa, the 316SS + Pt alloy exhibits a significantly lower total crack length over the strain-to-failure than the 316SS alloy.

(ii) Hafnium addition is very effective in suppressing post-irradiation IGSCC. No IG cracking was observed

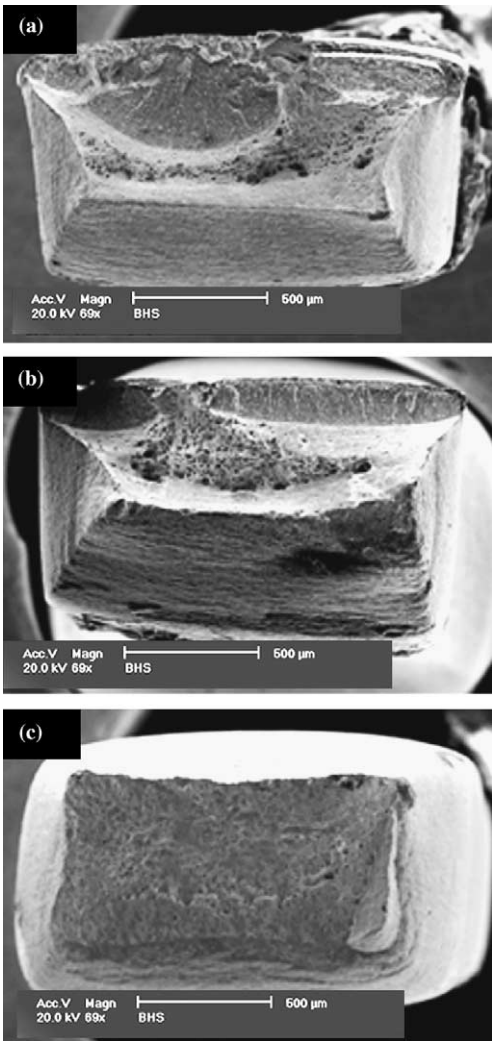

Fig. 8. SEM micrographs of the fracture surface of: (a) 316SS, (b) 316SS + Pt and (c) 316SS + Hf alloys proton-irradiated to 5 dpa at 400 °C and strained in simulated BWR NWC at 288 °C. The irradiated surface is the top surface in all micrographs.

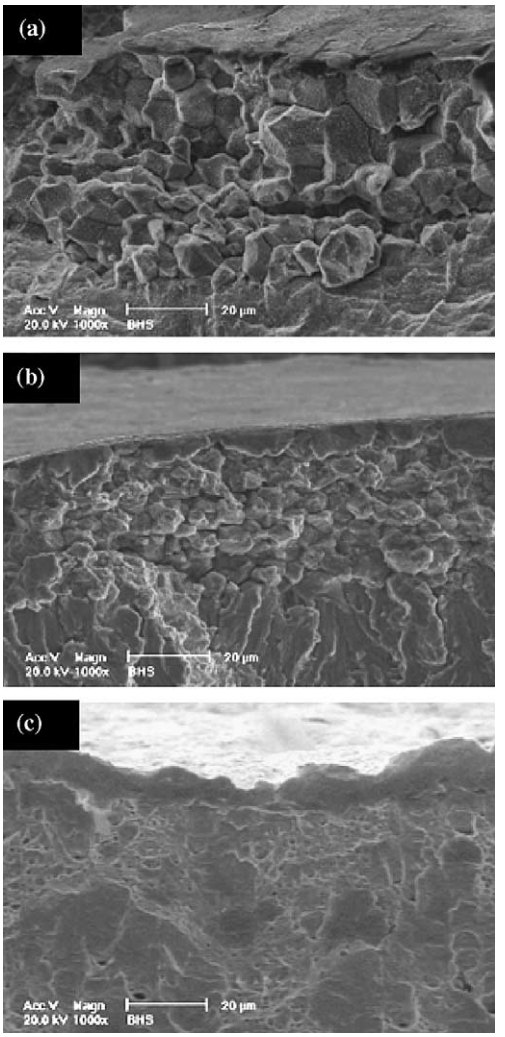

Fig. 9. High magnification SEM micrographs of the fracture surface of: (a) 316SS, (b) 316SS + Pt and (c) 316SS + Hf alloys proton-irradiated to 5 dpa at 400 °C and strained in simulated BWR NWC at 288 °C. The irradiated surface is the top surface in all micrographs. Notice IG cracking for 316SS alloy and 316SS + Pt alloy.

after CERT testing on a 316SS + Hf sample irradiated to 2.5 dpa. The 316SS + Hf sample at 2.5 dpa also exhibited an 8% ductility improvement in comparison to the 316SS alloy proton-irradiated to 2.5 dpa. Post-irradiation IGSCC is also suppressed in the 316SS + Hf alloy proton-irradiated to 5 dpa. At both 2.5 and 5 dpa, the total crack length over the strain-to-failure for the 316SS + Hf alloy is much lower than for the 316SS and 316SS + Pt alloys.

4. Discussion

In this study, Hf and Pt oversized solute atom additions to 316SS were clearly shown to have an impact on radiation-induced microstructure, radiation-induced hardening, radiation-induced microchemistry at grain boundaries and post-irradiation IGSCC resistance. This effect of oversized solute addition on radiation-induced damage is in general agreement with the findings of other studies [4–11,15]. Gan et al. [15] have investigated the effect of Pt and Hf oversized solute addition on the radiation-induced microstructure of the same alloys studied in this work, irradiated with Ni-ions at 500 °C up to 50 dpa. The dose dependencies of faulted loop density, faulted loop size, void density, void size and swelling for 316SS, 316SS + Pt and 316SS + Hf

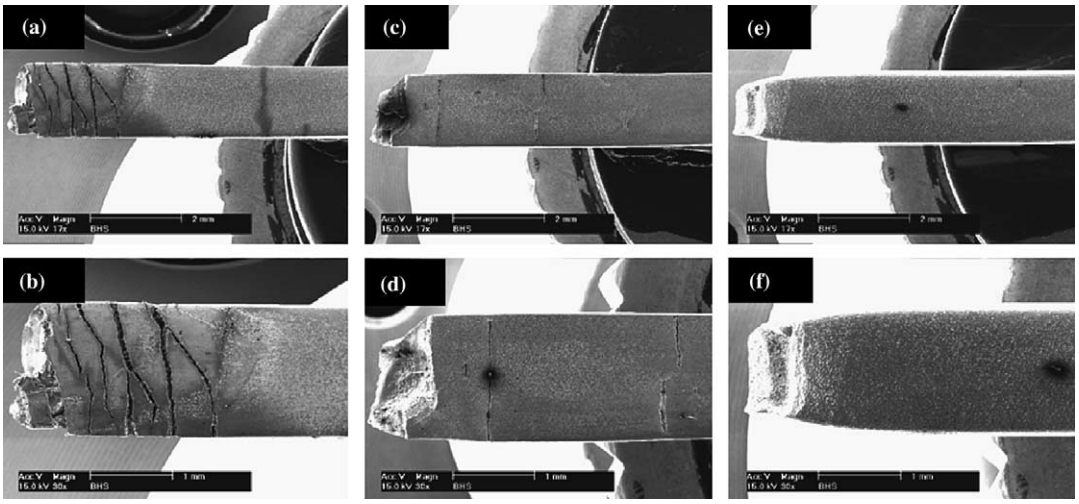

Fig. 10. SEM micrographs of the side surface of (a)–(b) 316SS alloy proton-irradiated to 5 dpa at 400 °C, (c)–(d) 316SS + Pt alloy proton-irradiated to 5 dpa at 400 °C and (e)–(f) 316SS + Hf alloy proton-irradiated to 5 dpa at 400 °C, strained in simulated BWR NWC at 288 °C.

irradiated with protons and Ni-ions up to 10 dpa are plotted in Figs. 11–15, respectively. In good agreement with proton-irradiation at 2.5 dpa, Pt addition is shown to increase faulted loop density and faulted loop size relative to the base alloy in Ni-ion irradiated specimens in the dose range 2–10 dpa. Also in good agreement with proton-irradiation data, Ni-ion irradiation produces a higher void density and void size in the 316SS + Pt alloy,

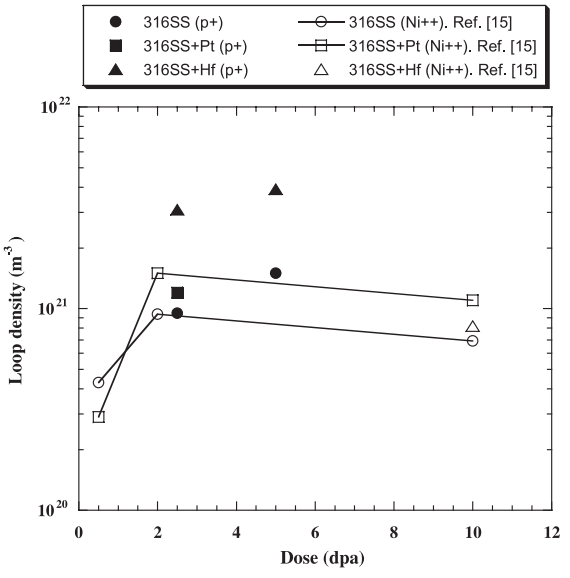

Fig. 11. Dose dependence of faulted loop density in 316SS, 316SS + Pt and 316SS + Hf alloys Ni-ion-irradiated at 500 °C and proton-irradiated at 400 °C. Ni-ion data are taken from Ref. [15].

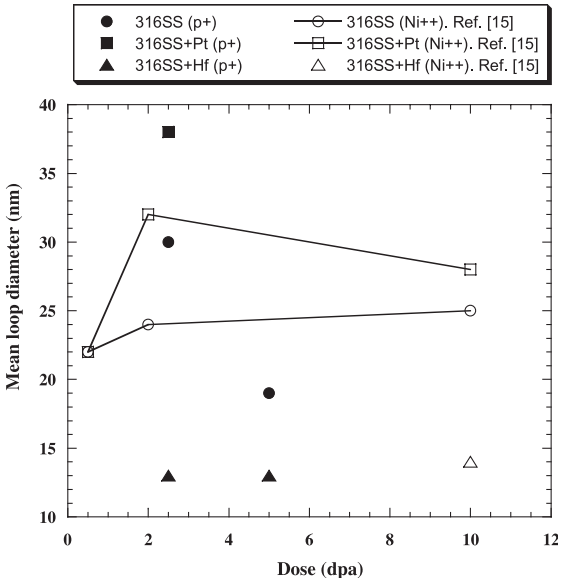

Fig. 12. Dose dependence of mean loop diameter in 316SS, 316SS + Pt and 316SS + Hf alloys Ni-ion-irradiated at 500 °C and proton-irradiated at 400 °C. Ni-ion data are taken from Ref. [15].

resulting in increased swelling, in comparison to the 316SS alloy in the dose range 2–10 dpa. Finally, the 316SS + Hf alloy Ni-ion-irradiated to 10 dpa also exhibits a much smaller faulted loop size (14 nm) than the 316SS alloy to 10 dpa (25 nm). Gan et al. already discussed in detail the effect of Pt and Hf oversized solute additions on the radiation-induced microstructure by

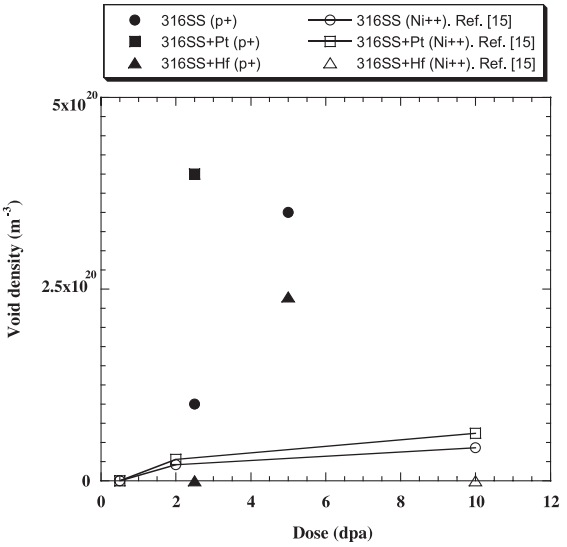

Fig. 13. Dose dependence of void density in 316SS, 316SS + Pt and 316SS + Hf alloys Ni-ion-irradiated at 500 °C and proton-irradiated at 400 °C. Ni-ion data are taken from Ref. [15].

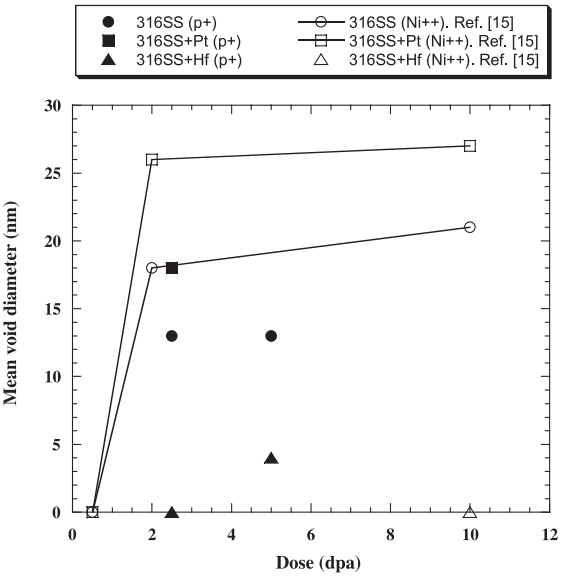

Fig. 14. Dose dependence of mean void diameter in 316SS, 316SS + Pt and 316SS + Hf alloys Ni-ion-irradiated at 500 °C and proton-irradiated at 400 °C. Ni-ion data are taken from Ref. [15].

comparing proton-irradiation and Ni-ion-irradiation data in Ref. [15]. Important conclusions of that study were the following: the effect of oversized solute addition is mainly on point defects kinetics rather than in-cascade processes, and the beneficial effect of Hf addition on

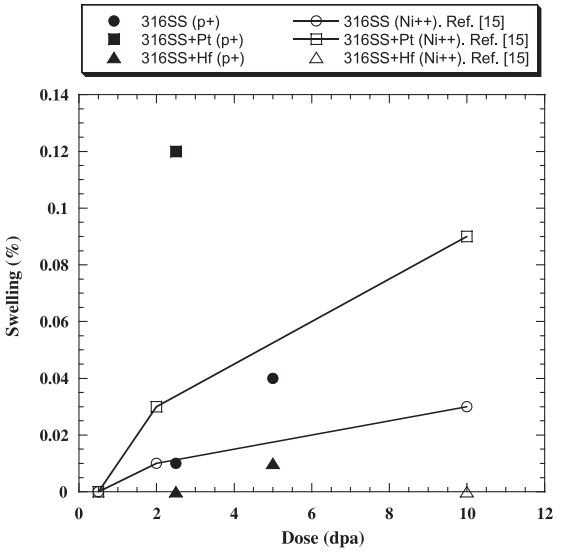

Fig. 15. Dose dependence of swelling in 316SS, 316SS + Pt and 316SS + Hf alloys Ni-ion-irradiated at 500 °C and proton-irradiated at 400 °C. Ni-ion data are taken from Ref. [15].

radiation-induced microstructure is due to solute atoms in the matrix.

On the basis of these conclusions drawn by Gan et al. [15], the following discussion will be focused on (i) the mechanisms by which oversized solute addition affect point defect behavior and (ii) the link between radiation-induced damage and post-irradiation IGSCC that may contribute to a better understanding of IASCC.

4.1. Influence of oversized solute addition on point defect behavior

The experimental results presented above showed that Hf addition effectively suppresses both RIS and void nucleation and also significantly reduces faulted loop growth at 2.5 dpa during proton irradiation. Interestingly the addition of the same amount of Pt has a similar effect on RIS but promotes void nucleation and leads to an increase in the density and the mean diameter of faulted loops at 2.5 dpa. This difference suggests that Pt and Hf impact point defect behavior by different mechanisms.

4.1.1. Influence of hafnium

Several authors [4–11] have suggested that oversized solute additions may reduce point defect migration to the grain boundary and agglomeration into loops and voids by trapping migrating vacancies and subsequently increasing the recombination rate. The results of this study on proton-irradiated 316SS + Hf are in good agreement with this mechanism.

Sakaguchi et al. [7] considered that the oversized solute atoms interact with vacancies via the formation of an additive-vacancy complex. These authors modeled the influence of the linear size factor of the oversized solute atoms on RIS. The linear size factor, L_{sf}, was defined as

$$L_{sf} = \{(\Omega_{add}/\Omega_{sol})^{1/3} - 1\} \times 100\ (\%), \quad (4)$$

where Ω_{sol} is the atomic volume of the solvent, and Ω_{add} is the atomic volume of the additive. Calculated linear size factors for various oversized solute atoms, including Pt and Hf, are given in Table 6. The amount of segregation was observed to decrease linearly with increases in the linear size factor of the oversized solute atoms. Model predictions were in good agreement with RIS measurements performed by Kato et al. [8] on model 316L stainless steel alloys doped with different oversized solute atoms and electron irradiated to 10.8 dpa at 500 °C. On the basis of this comparison, Sakaguchi et al. [7] concluded that the additive-vacancy binding energy is correlated with the linear size factor and controls the influence of oversized solute atom addition on RIS.

The formation of Hf-vacancy complexes and the subsequent enhancement of point defect recombination is a plausible mechanism as it would result in a reduction in the partitioning of point defects to faulted loops and voids and a reduction in the point defect flux to grain boundaries. This mechanism may explain the nearly complete suppression of RIS observed in the 316SS + Hf alloy proton-irradiated to 2.5 dpa and the reduction in the amount of RIS observed in the 316SS + Hf alloy at 5 dpa. It may also explain the reduction of faulted loop growth and the reduction in swelling observed in 316SS + Hf alloy.

4.1.2. Influence of platinum

While Hf and Pt additions have a similar influence in suppressing RIS, they have opposite effects on the radiation-induced microstructure. As shown in Section 3, Hf addition restricts the growth of loops and voids while Pt addition promotes loop growth and void nucleation. These results suggest that Pt solute atoms impact point defect behavior quite differently than Hf and do not enhance point defect recombination.

Table 6
Calculated linear size factor for various oversized solute elements

Element	Atomic number	Atomic mass (g)	Density ($g\,cm^{-3}$)	Atomic volume (cm^{-3})	Linear size factor (%)
V	23	50.94	6.09	8.36	6.81
Pt	78	195.08	21.45	9.09	9.84
Ti	22	47.88	4.51	10.62	15.68
Nb	41	92.91	8.58	10.83	16.44
Ta	73	180.95	16.68	10.85	16.51
Zr	40	91.23	6.51	14.01	26.87
Hf	72	178.46	13.31	13.41	25.04

The influence of different oversized solute atoms on radiation-induced changes in austenitic stainless steels has already been reported by Kato et al. [8]. These authors showed that the linear size factor of the oversized solute atoms strongly influences the concentration of point defects consumed in the matrix either by recombination or by agglomeration into loops and voids, and on the net flux of point defects towards grain boundaries. The results of their observations are presented in Fig. 16. In this work, RIS is thought to be controlled by the flux of point defects toward the grain boundary as influenced by two competitive mechanisms: (i) the formation of secondary defects (loops and voids) and (ii) the recombination of point defects.

- The formation of secondary defects is responsible for the decreased amount of RIS observed for oversized solute atoms with small linear size factors (vanadium, titanium). The result of our study on the effect of Pt is in good agreement with this idea.
- The recombination of point defects is responsible for the suppression of RIS by oversized solute atoms with large linear size factors (e.g. Hf and Zr). The flux of point defects to grain boundaries is maximum for oversized solute atoms with an intermediate linear size factor (niobium), which explains the evolution of chromium depletion at grain boundaries as a function of the linear size factor of additives plotted in Fig. 16(a).

A direct explanation for the difference between the effect of Hf and Pt oversized solute addition on radiation-induced microstructure is not obvious. The interaction between Pt oversized solute atoms and point defects seems to result in a reduction of the vacancy and interstitial diffusion rates rather than, as for the case of Hf addition, in an increase in their recombination rate. A reduction in the vacancy and interstitial diffusion rates and influence on subsequent aggregation may account for the suppression of RIS and the promotion of swelling and faulted loop growth. It is also consistent with the recent results of Allen et al. [22] showing that alloys with faster vacancy diffusion, that are prone to significant RIS, have a slower void nucleation rate, a longer transient swelling period, and less swelling.

4.2. IASCC mechanism

4.2.1. Role of RIS

RIS of major elements (Cr, Ni, Fe) and the resultant local depletion of Cr in austenitic stainless steels are

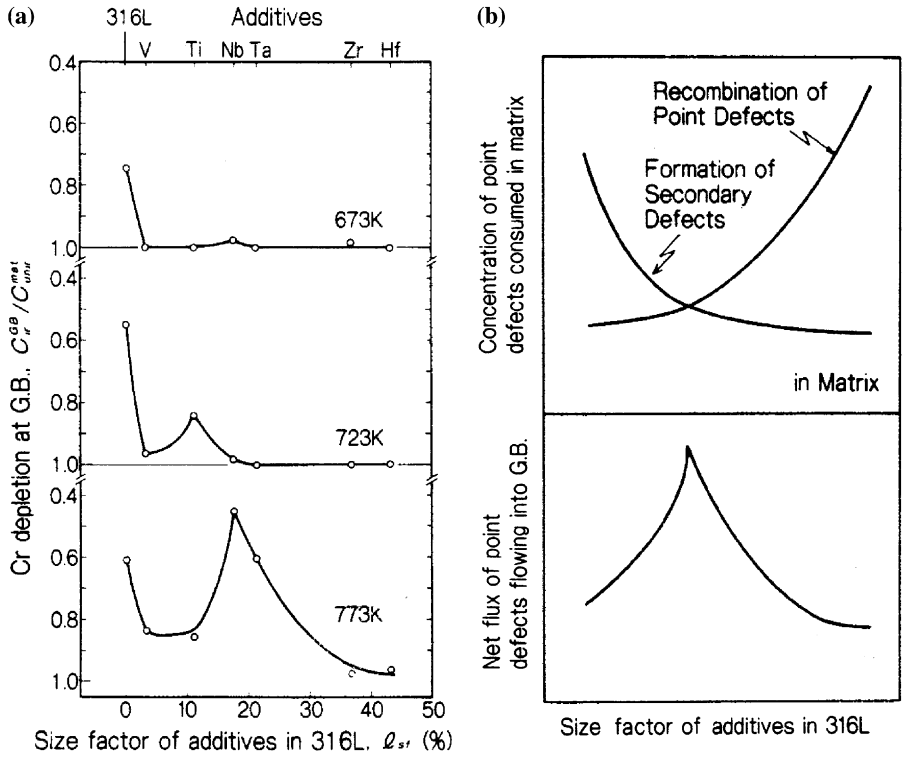

Fig. 16. (a) Changes in chromium depletion at grain boundaries in model additive-modified 316L stainless steel alloys with increasing linear size factor of additives after electron irradiation to 10.8 dpa, (b) schematic of the influence of the linear size factor of additives on the concentration of point defects consumed in the matrix and on the net flux of point defects towards grain boundaries. Taken from Kato et al. [8].

often considered as possible contributors to IASCC in BWR NWC. As shown in Table 4 and in Fig. 4, strong RIS occurs in the 316SS alloy at 2.5 dpa while RIS is suppressed in the 316SS + Hf alloy at 2.5 dpa. This is consistent with CERT tests showing resistance to post-irradiation IGSCC in the Hf doped alloy at 2.5 dpa. It is therefore tempting to attribute IASCC to RIS.

However, the results of RIS measurements and post-irradiation SCC tests on (i) 316SS alloy and 316SS + Pt alloy proton-irradiated to 2.5 dpa and (ii) on 316SS alloy and 316SS + Hf proton-irradiated to 5 dpa provide further insight into the effect of RIS on IASCC.

- As shown in Table 4 and in Fig. 4, strong RIS of major elements occurs in the 316SS alloy proton-irradiated to 2.5 dpa while RIS is minor in the 316SS + Pt alloy. However, in contrast to the 316SS + Hf alloy, both 316SS and 316SS + Pt alloys are found to be susceptible to post-irradiation IGSCC after proton-irradiation to 2.5 dpa.
- Also, both 316SS and 316SS + Hf alloys proton-irradiated to 5 dpa exhibit RIS at grain boundaries. Interestingly, the 316SS + Hf alloy proton-irradiated to 5 dpa remains highly resistant to post-irradiation IGSCC while, as expected, the 316SS alloy proton-irradiated to 5 dpa exhibits a higher degree of susceptibility to post-irradiation IGSCC than at 2.5 dpa. In addition, RIS for the 5 dpa 316SS + Hf sample is greater than the 2.5 dpa 316SS + Pt sample that was susceptible to IGSCC.

These results illustrate that RIS of major elements in austenitic stainless steels is not the only factor promoting IASCC in BWR NWC.

A recent study by Busby et al. [23] led to the same conclusion. The authors determined the post-irradiation annealing heat treatment conditions that removed either microstructural or microchemical damage while leaving the other unaffected. Both high-purity 304L and commercial purity 304SS alloys were irradiated with 3.2 MeV protons at 360 °C to doses up to 2.5 dpa. Post-irradiation anneals were performed at temperatures ranging from 400 to 650 °C for times between 45 and 90 min. Annealing at 600 °C for 90 min was found to remove virtually all dislocation loops while leaving RIS virtually unchanged. The specimen strained in simulated BWR

NWC after annealing at 600 °C for 90 min did not exhibit any IG cracking, indicating that RIS of major elements is not the only cause of IASCC. This same study reviewed the results of several experiments with neutron-irradiated alloys that agreed with the results of the post-irradiation annealing study on proton-irradiated alloys.

RIS of minor elements (Mo, Mn and Si) in these high-purity alloys cannot account for IASCC. Indeed, no significant radiation-induced changes in the microchemistry of these minor alloying elements were detected in this work for the 316SS + Pt alloy proton-irradiated to 2.5 dpa while this alloy was found to be susceptible to post-irradiation IGSCC.

4.2.2. Role of radiation-induced hardening

Radiation-induced hardening is also considered to play a major role in IASCC. The ratio of total crack length to failure strain as a function of the yield stress is plotted in Fig. 17 for the 316SS, 316SS + Pt, and 316SS + Hf alloys proton-irradiated to 2.5 and 5 dpa and then strained in simulated BWR NWC. The total crack length over the strain-to-failure shows a reasonable linear dependence with the yield stress independent of the material for proton-irradiated 316SS, 316SS + Pt and 316SS + Hf alloy. The only exception is the data corresponding to the 316SS + Hf alloy at 5 dpa that did not exhibit measurable post-irradiation stress corrosion crack initiation.

The important role of the yield stress on stress corrosion crack growth of both irradiated and non-irradiated stainless steel in BWR type water has been emphasized by Andresen [24]. On the basis of the hypothesis that the primary role of radiation-induced hardening is to increase the yield stress, Andresen compared the stress corrosion crack growth behavior of irradiated stainless steel and cold work non-irradiated stainless steel. Results of this work showed that radiation-induced hardening and cold work produce similar effects on SCC growth rate, suggesting that the yield stress controls the SCC growth of both irradiated and non-irradiated stainless steels.

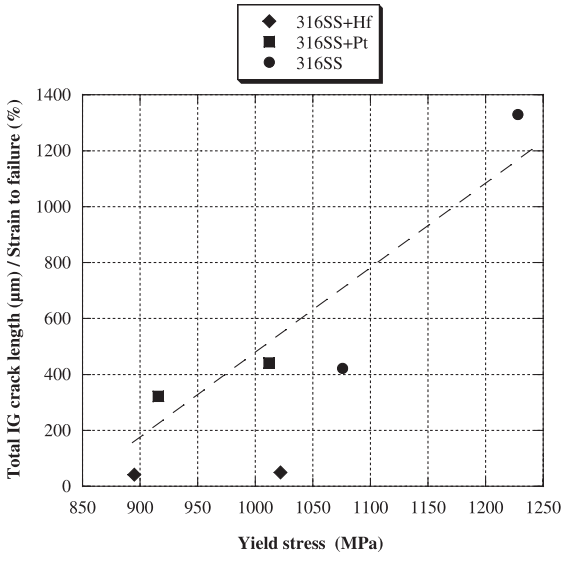

Fig. 17. Evolution of the ratio of total IG crack length to failure strain as a function of the yield stress for 316SS, 316SS + Pt and 316SS + Hf alloys proton-irradiated at 400 °C.

While the increase in the yield stress due to irradiation seems to play a major role in IASCC growth, the mechanisms by which irradiation leads to hardening is still not well understood. The dispersed hardening model [25] derived from the Orowan mechanism [26] is often used in order to compare hardness measurements with the density and the mean diameter of faulted loops obtained after TEM examination in the case of irradiated materials. As already mentioned in the results section, the prediction of the dispersed hardening model led to significant underestimation of the radiation-induced hardening measured in this work.

Several authors [27–29] have considered the source hardening model as an alternative model to the dispersed hardening model to explain radiation-induced hardening. In the source hardening model, clusters of small defects (self-interstitial atoms (SIA)) that cannot be resolved by TEM are believed to decorate the grown-in dislocations so that they cannot act as dislocation sources. Trinkaus et al. [28] suggested that this effect may arise from either migration and enhanced agglomeration of single SIA in the form of loops in the strain field of the dislocation, or glide and trapping of SIA loops (directly produced in the cascades) in the strain field of the dislocation. Detailed examination of the effect of such small defect clusters on both radiation-induced hardening and IASCC may lead to a better understanding of these complex phenomena.

5. Conclusions

The influence of 0.3 at.% of Pt and Hf oversized solute atoms on both radiation-induced changes and post-irradiation IGSCC behavior of high-purity model 316SS alloys proton-irradiated at 2.5 and 5 dpa was investigated. The main results of this work show that Pt and Hf have the following effects:

1. Both Pt and Hf additions suppress RIS. Pt and Hf additions lead to a significant suppression of RIS at 2.5 dpa. While less effective at 5 dpa, RIS in the Hf-doped alloy is still suppressed relative to the base alloy.

2. In contrast to the similar effects of Pt and Hf on RIS, Pt and Hf oversized solute atoms have opposite effects on the radiation-induced microstructure evolution. The addition of Hf is effective in suppressing swelling and loop growth. Pt addition appears to promote swelling and faulted loop development.
3. Both Pt and Hf additions reduce the degree of radiation hardening.
4. Both Pt and Hf additions have a beneficial effect on post-irradiation IGSCC in the simulated NWC of a BWR. Pt addition alters the extent of cracking during post-irradiation IGSCC tests at both 2.5 and 5 dpa. Remarkably, Hf addition completely suppresses post-irradiation IGSCC at both doses.

Overall, the results of this study demonstrate that oversized Hf solute and to a lesser extent Pt have beneficial impacts on both radiation-induced changes and post-irradiation IGSCC of austenitic stainless steels. The good agreement in the results on radiation-induced microstructure between proton-irradiated specimens and nickel-ion-irradiated specimens from the same alloys shows that oversized solute atoms mainly affect the microstructure through intracascade process. The mechanisms by which oversized solute atoms affect point defect behavior is difficult to assess. The results of this work demonstrate that these mechanisms are different for Pt and Hf oversized solute atoms. The effect of Pt is consistent with a mechanism that reduces the point defect diffusion rates and influences subsequent defects aggregation, while the Hf effect is consistent with a mechanism that increases the recombination rate of point defects possibly through the formation of additive-vacancy complexes.

Acknowledgements

The authors are grateful to V. Rotberg and O. Toader for their help in conducting proton irradiation at the University of Michigan Ion Beam Laboratory. We also thank S. Thevuthasan and V. Shutthanandan for nickel-ion irradiation carried out at Pacific Northwest National Laboratory and P. Andresen at General Electric Global Research for providing the HP alloys. Support was provided by the Nuclear Energy Research Initiative (NERI) program and the Office of Basic Energy Sciences, U.S. Department of Energy under contract DE-AC06-76RLO 1830 with Battelle Memorial Institute. Research at the Oak Ridge National Laboratory SHaRE User Facility was sponsored by the Division of Materials Sciences and Engineering, U.S. Department of Energy, under contract DE-AC05-00OR22725 with UT-Battelle, LLC, and through the SHaRE Program under contract DE-AC05-76OR00033 with Oak Ridge Associated Universities.

References

[1] P. Scott, J. Nucl. Mater. 211 (1994) 101.
[2] T. Shoji, S. Suzuki, K.S. Raja, J. Nucl. Mater. 258–263 (1998) 241.
[3] G.S. Was, P.L. Andresen, J. Met. (April) (1992) 8.
[4] H. Watanabe, T. Muroga, N. Yoshida, J. Nucl. Mater. 239 (1996) 95.
[5] N. Shigenaka, S. Ono, Y. Isobe, T. Hashimoto, H. Fujimori, S. Uchida, J. Nucl. Sci. Technol. 33 (7) (1996) 577.
[6] S. Kasahara, K. Nakata, K. Fukuya, S. Shima, A.J. Jacobs, G.P. Wozadlo, S. Suzuki, in: Proceedings of the Sixth International Symposium on Environmental Degradation of Materials in Nuclear Power, Systems – Water Reactors, 1–5 August, San Diego, CA, The Minerals, Metals & Materials Society, 1993, p. 615.
[7] N. Sakaguchi, S. Watanabe, H. Takahashi, Nucl. Instrum. and Meth. B 153 (1999) 142.
[8] T. Kato, H. Takahashi, M. Izumiya, J. Nucl. Mater. 189 (1992) 167.
[9] M.A. Ashworth, D.I.R. Norris, I.P. Jones, J. Nucl. Mater. 189 (1992) 289.
[10] S. Ohnuki, S. Yamashita, H. Takahashi, T. Kato, in: Proceedings of the 19th International Symposium on the Effects of Radiation on Materials, 16–18 June, Seattle, WA, American Society for Testing and Materials, 1999, p. 756.
[11] S. Dumbill, W. Hanks, in: Proceedings of the Sixth International Symposium on Environmental Degradation of Materials in Nuclear Power Systems – Water Reactors, 1–5 August, San Diego, CA, The Minerals, Metals & Materials Society, 1993, p. 521.
[12] E.D. Eason, Development, Evaluation, and Analysis of the Initial CIR-IASCC Database, EPRI Report TR-108749, 1998.
[13] G.S. Was, J.T. Busby, T. Allen, E.A. Kenik, A. Jenssen, S.M. Bruemmer, J. Gan, A.D. Edwards, P.M. Scott, P.L. Andresen, J. Nucl. Mater. 300 (2002) 198.
[14] J. Gan, E.P. Simonen, D.J. Edwards, S.M. Bruemmer, L. Fournier, B.H. Sencer, G.S. Was, Proceedings of the Materials Research Society Meeting, Boston, MA, 2000.
[15] J. Gan, E.P. Simonen, S.M. Bruemmer, L. Fournier, B.H. Sencer, G.S. Was, J. Nucl. Mater., in press.
[16] D.L. Damcott, J.M. Cookson, R.D. Carter Jr., J.R. Martin, M. Atzmon, G.S. Was, Radiat. Eff. Def. Solids 118 (1991) 383.
[17] Standard practice for neutron radiation damage simulation by charged-particle irradiation, ASTM Designation E 521-89, Annual Book of ASTM Standards, vol. 12.02, American Society for Testing and Materials, Philadelphia, PA, 1989, p. D-9.
[18] M.L. Jenkins, J. Nucl. Mater. 216 (1994) 124.
[19] J. Gan, G.S. Was, J. Nucl. Mater. 297 (2001) 161.
[20] H.R. Higgy, F.H. Hammad, J. Nucl. Mater. 55 (1975) 177.
[21] E.P. Simonen, R.H. Jones, S.M. Bruemmer, J. Nucl. Mater. 191–194 (1992) 1002.
[22] T.R. Allen, J.T. Busby, E.A. Kenik, G.S. Was, in: Proceedings of the 19th International Symposium on the Effects of Radiation on Materials, 16–18 June, Seattle, WA, American Society for Testing and Materials, 1999, p. 739.

[23] J.T. Busby, G.S. Was, E.A. Kenik, J. Nucl. Mater. 302 (2002) 20.
[24] P.L. Andresen, Corrosion 2002, 7–11 April, Denver, CO, National Association of Corrosion Engineers, 2002, p. 17.
[25] A. Seeger, Proceedings of the 2nd United Nations International Conference on Peaceful Uses of Atomic Energy, vol. 6, Geneva, September, 1958, p. 250.
[26] E. Orowan, Nature 149 (1992) 643.
[27] B.N. Singh, A.J.E. Foreman, H. Trinkaus, J. Nucl. Mater. 249 (1997) 103.
[28] H. Trinkaus, B.N. Singh, A.J.E. Foreman, J. Nucl. Mater. 251 (1997) 172.
[29] D. Rodney, G. Martin, Phys. Rev. B 61 (13) (2000) 8714.